JOURNAL OF COMPUTATIONAL PHYSICS 107, 338–347 (1993)

A Boundary Element Model of Cathodic Well Casing Protection

S. H. LEE, D. W. TOWNLEY, AND K. O. ESHUN

Chevron Oil Field Research Company, P.O. Box 446, La Habra, California 90633-0446

Received January 21, 1992

An efficient boundary element method was developed to study cathodic protection of a well casing in a formation with layered conductivities. Even though the electrical potential in soil is governed by the linear Laplace equation, electrochemical reactions at the well casing introduce complex, nonlinear boundary conditions. Furthermore, the complexity of boundary geometries makes the numerical computation nontrivial. Use of Green's function allows a general solution of the Laplace equation to be expressed in the form of a Fredholm integral equation of the second kind. The present formula employs a fundamental solution that eliminates the discretization of the top ground surface. Because the potential distribution within the well casing metal greatly affects the current distribution, the model includes the potential change along the axial direction of the well casing. A Newton-Raphson method was employed to estimate iteratively the current distribution at the well casing, and then the integral equations of the boundary element method were numerically solved by a collocation technique. This boundary element model was used to investigate the effects of soil conductivities, well casing geometry, well casing resistivity, and the location of a current source on the current and potential distribution at the well casing.

1. INTRODUCTION

Cathodic protection is often employed to prevent external corrosion of oil production well casings. The negative terminal of a direct current power source is connected to the casing at the wellhead, while the positive terminal is connected to an auxiliary buried structure called the anode or groundbed. Current is discharged from the anode, flows through the soil, and is picked up on the well casing. The distribution of current density on the well casing determines the degree of corrosion protection. Current flow through the soil is governed by Laplace's equation, while electrochemical kinetics describes the current discharge at the anode and pickup at the cathode.

The total current required to protect a casing cannot be predicted with any certainty from simple rules of thumb, nor can surface measurements alone determine the level of protection at the bottom of the casing. The actual protection level along the well bore can be directly measured with downhole tools, but this is expensive both in direct cost and in lost production.

Several methods have been used to model well casings to predict current requirements. Pope [1] first used a simple electrical transmission line model assuming that the soil resistivity and electrochemical kinetics generate a constant attenuation coefficient. While this assumption has been used and is often reasonable for well-coated horizontal pipelines, it is rarely accurate for a well casing. Schremp and Newton [2] modified this early model to include a semi-empirical relationship between attenuation coefficient and depth. More recently Dabkowski [3] improved the model by calculating the attenuation coefficient for each segment from the local soil conductivity, local electrochemical kinetics, and the geometry of the casing–groundbed system.

Because all the phenomena of interest in cathodic protection occur on surfaces, the boundary element method is a natural approach to this problem. Applications of the boundary element method have been commonly limited to homogeneous physical systems with linear governing equations. Nevertheless, it has been successfully applied in a variety of fields, for example, solid mechanics [4, 5], low-Reynolds-number fluid motion [6, 7], ground water flow [8], and well productivity calculation [9]. The boundary element method has three distinct advantages over the conventional finite-difference or -element method in calculating an electrical field. First, the potential strengths at the boundary elements are directly calculated. Therefore, only the boundaries must be discretized, which renders great flexibility and convenience in describing boundary surfaces. Secondly, the order of spatial dimensionality for the flow problem is reduced: three-dimensional problems become two-dimensional (surface) integral equations, and two-dimensional problems become one-dimensional (line) integral equations. Consequently, the boundary element method is more efficient in computation and requires less memory storage than a finite-difference or -element method. Finally, the potential strengths at the boundaries are not subject to cumulative errors through a three-dimensional grid. Because the boundary conditions for this problem are

0021-9991/93 $5.00

quite stiff, small errors in potential strength incur large errors in current density distribution.

The boundary element method has been used extensively for modeling corrosion of structures in sea water [10–13]. In these previously modeled systems, the resistivity of the corrosive medium is constant. This paper extends the use of the boundary element method to systems where the resistivity is layered and also incorporates realistic, nonlinear boundary conditions at the well casing into iterative computation. The present formulation employs the Green's function appropriate to the planar ground surface. Furthermore, the algorithm is designed to solve a large system efficiently.

In Section 2 a general solution of Laplace's equation is formulated in terms of boundary integrals, and the nonlinear boundary conditions at the well casing are specified. Section 3 describes an iterative numerical scheme to solve this nonlinear problem. In Section 4 some numerical examples are included to discuss the effects of conductivities of soil, well casing geometry, well casing resistivity, and the location of the current source on cathodic well casing protection. Finally, conclusions follow in Section 5.

2. FORMULATION

A schematic diagram of the cathodic well casing protection system is illustrated in Fig. 1. The groundbed (anode) is small compared with the well casing and is considered to be a point current source at $\mathbf{x}_0 = (x_0, y_0, z_0)$. Note that the conductivity of the well casing is generally much larger than that of soil (e.g., $10^5[1/\Omega m]$ vs. $0.1[1/\Omega m]$) and the well casing length is several orders of magnitude greater than the casing diameter (e.g., 1000 $[m]$ vs. 0.16 $[m]$). The boundary integral equations for an electrical field in a semi-infinite domain with layered conductivities are derived because the top ground surface is planar.

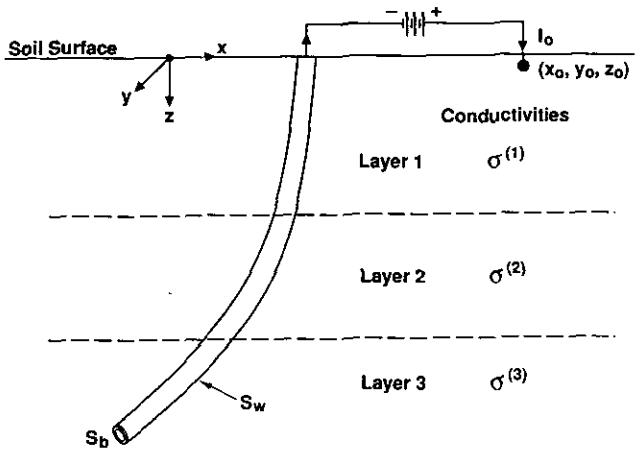

FIG. 1. A schematic diagram of cathodic well casing protection.

2.1. *A General Solution for Electrical Field in a Semi-infinite Domain*

The electrical current is proportional to the potential gradient,

$$\mathbf{i} = -\sigma \nabla \phi, \tag{1}$$

where $\mathbf{i}$ is the current, σ is the formation conductivity, and ϕ is the potential.

The equation of current conservation is given by

$$\nabla \cdot \mathbf{i} = \sigma f(\mathbf{x}). \tag{2}$$

Here, f is a source term in the domain.

The divergence of Eq. (1) yields Laplace's equation for potential,

$$\nabla^2 \phi = -f(\mathbf{x}). \tag{3}$$

Note that the potential field is solved in a semi-infinite domain, and the boundary condition at $z = 0$ (the soil surface) includes $\mathbf{i} \cdot \mathbf{n} = 0$. Thus, instead of the usual Green's function for Laplace's equation [14], we use a special fundamental solution that makes the general solution automatically satisfy the boundary conditions at $z = 0$ (a similar approach was taken for a Stokes problem in Ref. [15]).

$$q(\mathbf{x}, \mathbf{y}) = \frac{1}{4\pi}\left[\frac{1}{|\mathbf{x}-\mathbf{y}|} + \frac{1}{|\mathbf{x}-2x_3\mathbf{e}_3-\mathbf{y}|}\right]. \tag{4}$$

Here, $\mathbf{x}$ and $\mathbf{y}$ are position vectors. The components of $\mathbf{x}$ in the xyz coordinates are given by (x_1, x_2, x_3) and the unit vectors are denoted by $\mathbf{e}_1, \mathbf{e}_2$, and $\mathbf{e}_3$. The fundamental solution is equivalent to the sum of the solutions due to point sources at $\mathbf{x}$ and $\mathbf{x} - 2x_3\mathbf{e}_3$, which will eliminate the discretization of the plane at $z = 0$. Using Green's thereom, a general solution of Eq. (3) can be readily expressed in the form of a Fredholm integral equation of the second kind,

$$\phi(\mathbf{x}) = -\iiint q(\mathbf{x}, \mathbf{y}) f(\mathbf{y})\, dV_y + \iint q(\mathbf{x}, \mathbf{y}) \frac{\partial \phi}{\partial n}(\mathbf{y})\, dS_y$$

$$- \iint \nabla_y q(\mathbf{x}, \mathbf{y}) \cdot \mathbf{n}\phi(\mathbf{y})\, dS_y, \tag{5}$$

where

$$\nabla_y q(\mathbf{x}, \mathbf{y}) = \frac{1}{4\pi}\left[\frac{(\mathbf{x}-\mathbf{y})}{|\mathbf{x}-\mathbf{y}|^3} + \frac{(\mathbf{x}-2x_3\mathbf{e}_3-\mathbf{y})}{|\mathbf{x}-2x_3\mathbf{e}_3-\mathbf{y}|^3}\right]. \tag{6}$$

The S in the integral is the boundaries of the domain, V, and

$\mathbf{n}$ is an exterior normal at the boundaries of V. The current is easily obtained as the gradient of Eq. (5),

$$\frac{1}{\sigma}\mathbf{i}(\mathbf{x}) = \iiint \nabla_x q(\mathbf{x}, \mathbf{y}) f(\mathbf{y})\, dV_y - \iint \nabla_x q(\mathbf{x}, \mathbf{y}) \frac{\partial \phi}{\partial n}(\mathbf{y})\, dS_y + \iint \nabla_x \nabla_y q(\mathbf{x}, \mathbf{y}) \cdot \mathbf{n}\phi(\mathbf{y})\, dS_y. \tag{7}$$

Here,

$$\nabla_x q(\mathbf{x}, \mathbf{y}) = -\frac{1}{4\pi}\left[\frac{(\mathbf{x}-\mathbf{y})}{|\mathbf{x}-\mathbf{y}|^3} + \frac{(\mathbf{x}-\mathbf{I}_3\cdot\mathbf{y})}{|\mathbf{I}_3\cdot\mathbf{x}-\mathbf{y}|^3}\right], \tag{8}$$

$$\nabla_x \nabla_y q(\mathbf{x}, \mathbf{y}) = \frac{1}{4\pi}\left[\frac{\mathbf{I}}{|\mathbf{x}-\mathbf{y}|^3} + \frac{\mathbf{I}_3}{|\mathbf{I}_3\cdot\mathbf{x}-\mathbf{y}|^3} - \frac{3(\mathbf{x}-\mathbf{y})(\mathbf{x}-\mathbf{y})}{|\mathbf{x}-\mathbf{y}|^5} - \frac{3(\mathbf{I}_3\cdot\mathbf{x}-\mathbf{y})(\mathbf{x}-\mathbf{I}_3\cdot\mathbf{y})}{|\mathbf{I}_3\cdot\mathbf{x}-\mathbf{y}|^5}\right]. \tag{9}$$

Furthermore,

$$\mathbf{I} = \begin{pmatrix} 1 & 0 & 0 \\ 0 & 1 & 0 \\ 0 & 0 & 1 \end{pmatrix} \quad \text{and} \quad \mathbf{I}_3 = \begin{pmatrix} 1 & 0 & 0 \\ 0 & 1 & 0 \\ 0 & 0 & -1 \end{pmatrix}.$$

The two surface integrals on the right-hand sides of Eq. (5) are known as the single-layer and double-layer potentials, respectively. Note that $\partial\phi/\partial n$ and ϕ, acting as the density functions for these potentials at the boundaries, determine the potential field throughout the entire domain. Hence, the general solution (5) should be applied at the boundaries in order to determine the unknown values of ϕ and/or $\partial\phi/\partial n$ at the boundaries.

Single-layer potentials are continuous in the entire domain, including boundaries. However, double-layer potentials are not continuous but suffer a jump [16]. Hence, if we define the function $W(\mathbf{x})$ as the double-layer potential by

$$W(\mathbf{x}) \equiv -\frac{1}{4\pi}\iint\left[\frac{(\mathbf{x}-\mathbf{y})}{|\mathbf{x}-\mathbf{y}|^3} + \frac{(\mathbf{x}-2x_3\mathbf{e}_3-\mathbf{y})}{|\mathbf{x}-2x_3\mathbf{e}_3-\mathbf{y}|}\right] \cdot \mathbf{n}\phi(\mathbf{y})\, dS_y, \tag{10}$$

the jump condition can be expressed in the simple form

$$W^i(\mathbf{x}) = \tfrac{1}{2}\phi(\mathbf{x}) + W^s(\mathbf{x}) \tag{11}$$

with $\mathbf{x}$ in the interior of V, and

$$W^e(\mathbf{x}) = -\tfrac{1}{2}\phi(\mathbf{x}) + W^s(\mathbf{x}) \tag{12}$$

with $\mathbf{x}$ in the exterior of V.

Here, $W^i(\mathbf{x})$ and $W^e(\mathbf{x})$ denote the limiting values of $W(\mathbf{x})$ approached from inside and outside the domain V, respectively. Also $W^s(\mathbf{x})$ denotes $W(\mathbf{x})$ evaluated at $\mathbf{x} \in S$.

It should be noted that the general integral Eq. (5) is of lower order in spatial dimension than the original partial differential Eq. (3) (i.e., surface integrals for a three-dimensional problem). Often, the values of the potential density functions, $\partial\phi/\partial n$ and ϕ, at the boundaries are the only desired information. Hence, the boundary integral method may be more efficient than a finite-difference method or a finite-element method, which requires solution of Eq. (3) throughout the entire domain in order to evaluate the potential and flux distributions at the boundaries.

2.2. *Boundary Conditions*

In each domain there are three types of boundaries: (1) Dirichlet boundaries, where ϕ is specified; (2) Neumann boundaries, where $\nabla\phi \cdot \mathbf{n}$ is specified; (3) common boundaries between two layers. The ground surface has the Neumann boundary condition ($\nabla\phi \cdot \mathbf{n} = 0$), but the general solution of Eq. (5) automatically satisfies the boundary conditons at $z = 0$ owing to the fundamental solution chosen.

The total current (I_0) from an anode in layer 1 can be written as a point source,

$$f(\mathbf{x}) = \frac{I_0}{\sigma^{(1)}}\delta(\mathbf{x}-\mathbf{x}_0). \tag{13}$$

The superscript (1) of σ denotes the soil conductivity in layer 1. The total current picked up on the well casing should also be I_0,

$$I_0 = \iint \mathbf{i}\cdot\mathbf{n}\, dS_w. \tag{14}$$

The integral is over the side surface of the well casing. At the well casing side surface (S_w), two separate electrochemical processes occur: an anodic dissolution of the metal and the corresponding reduction of electrolyte in the soil. As a result of these reactions, the boundary conditions are usually modeled by a nonlinear Tafel equation [17]:

$$\mathbf{i}\cdot\mathbf{n} = i^*(e^{(\phi_c-\phi_w-\phi^*)/\beta_a} - e^{-(\phi_c-\phi_w-\phi^*)/\beta_c}). \tag{15}$$

Here, ϕ_c and ϕ_w are the potentials at the well casing surface and in the formation next to the well casing, respectively. The i^*, ϕ^*, β_a, and β_c are parameters describing the elec-

trochemical kinetics. The boundary conditions given by Eq. (15) are generally stiff due to exponential functions.

Because the well casing is very long compared with its diameter, the potential will change due to the resistivity of the metal of the well casing. This potential change can be conveniently expressed as

$$\frac{d\phi_c}{dl} = -R_s \mathfrak{I}(l). \tag{16}$$

Here, R_s is the metal resistivity per unit length, and $\mathfrak{I}$ is the total current flowing up the casing at l,

$$\mathfrak{I}(l) = \int_l^L \int_0^{2\pi} \mathbf{i} \cdot \mathbf{n} \, dS_w. \tag{17}$$

The L is the total length of the casing. It should be noted that Eq. (16) approximates a two-dimensional surface distribution of eletrical potential at the well casing with a line distribution of potentials.

At the bottom surface of the well casing, the boundary condition of no current flow applies:

$$\mathbf{n} \cdot \nabla\phi = 0 \qquad \text{for} \quad \mathbf{x} \in S_b. \tag{18}$$

At the shared boundaries (S_L) between two layers (i.e., k and $k+1$), potential and normal current flux are continuous,

$$\phi^{(k)} = \phi^{(k+1)}, \tag{19}$$

$$\mathbf{n}^{(k)} \cdot \mathbf{i}^{(k)} = -\mathbf{n}^{(k+1)} \cdot \mathbf{i}^{(k+1)}. \tag{20}$$

Note that the direction of the exterior normal of layer $(k+1)$ is opposite to that of layer k at S_L.

3. NUMERICAL METHOD

When either Dirichlet or Neumann conditions are specified at each boundary, the governing integral equations of the boundary element method can be numerically solved by collocation for the unknown variables, ϕ or $\nabla_n\phi$. As discussed in the previous section, the current at the well casing is a nonlinear function of the potential difference between soil and well casing surface, and the total current flowing onto the well casing should be identical to the total current emitted from the point source in layer 1. These nonlinear boundary conditions and constraints obviously entail an iterative numerical scheme to solve this problem. An efficient numerical scheme, as a result, is derived for a model with N_L layers.

3.1. *A Collocation Method for Integral Equations*

By the use of the jump conditions of potential double layers at the boundary, Eqs. (11)–(12), the integral equation (5) is first reformulated for the unknown potentials or potential gradients at the boundaries. Then, the equation is solved by a zeroth-order collocation technique (i.e., constant potential and potential gradients in a discrete grid). Specifically, the boundary surfaces are divided into $N^{(k)}$ elements in layer k and the potential strengths (ϕ and $\nabla_n\phi$) are assumed constant within an element. The resulting system of discretized equations becomes

$$\frac{1}{2}\phi_i^{(k)} = -\delta_1^k q(\mathbf{x}, \mathbf{x}_0)\frac{I_0}{\sigma^{(1)}} + \sum_j q_{i,j}^{(k)} \nabla_n \phi_j^{(k)} - \sum_j \nabla_n q_{i,j}^{(k)} \phi_j^{(k)}, \qquad \text{for} \quad k = 1, \ldots, N_L \quad \text{and} \quad i, j = 1, \ldots, N^{(k)}. \tag{21}$$

Here, the superscript (k) denotes the variable in layer k, the subscripts i and j denote the grid points, δ is a Kronecker delta function, and

$$q_{i,j}^{(k)} \equiv \iint q^{(k)}(\mathbf{x}_i, \mathbf{y}) \, dS_{yj}, \tag{22}$$

$$\nabla_n q_{i,j}^{(k)} \equiv \iint \nabla_y q^{(k)}(\mathbf{x}_i, \mathbf{y}) \cdot \mathbf{n} \, dS_{yj}. \tag{23}$$

The surface integrals of Eqs. (22) and (23) are calculated by a Gaussian quadrature method [18]. When $j = i$, the integrands become unbounded. In this case the surface is subdivided into two regions, one of which is centered around the singular point. The integration in this subdivision is computed analytically [6, 9, 15].

The linear Eq. (21) can be concisely rewritten in a matrix formulation,

$$\mathbf{A}^{(k)} \cdot \mathbf{\Phi}^{(k)} + \mathbf{B}^{(k)} \cdot \nabla_n \mathbf{\Phi}^{(k)} = \mathbf{C}^{(k)} \qquad \text{for} \quad k = 1, \ldots, N_L. \tag{24}$$

At the shared boundaries (S_L) between two layers (i.e., k and $k+1$), the continuity of potential and current are given by

$$\phi_i^{(k)} = \phi_i^{(k+1)} \tag{25}$$

$$\nabla_n \phi^{(k+1)} = -\frac{\sigma^{(k)}}{\sigma^{(k+1)}} \nabla_n \phi^{(k)}. \tag{26}$$

3.2. *Boundary Conditions at the Well Casing*

When the well casing surface is divided into N_θ grids in the azimuthal direction and N_z grids in the axial direction,

it is convenient to represent the current and potential around the well casing from all the layers by arrays i^w_{mn} and ϕ^w_{mn} (for $m=1, ..., N_\theta$ and $n=1, ..., N_z$). The radius of the well casing is much smaller than the well length and the conductivity of the well casing is generally large. Therefore, the potential difference in the azimuthal direction on the well casing surface is negligible. The potential on the well casing surface is given as ϕ^c_j along the axial direction.

From Eqs. (16) and (17), the potential at the well casing surface can be easily computed as

$$\phi^c_j = \phi^c_0 - R_s \sum_{m \geqslant j} \Im_m \Delta l^w_m, \tag{27}$$

$$\Im_j \equiv \sum_{n=N_z}^{j} \sum_{m=1}^{N_\theta} i^w_{mn} \Delta S^w_{mn}. \tag{28}$$

The ϕ^c_0 is the potential at the bottom of the well casing; Δl^w_m is the axial length of the grid at $j=m$; and ΔS^w_{mn} is the surface area of the grid at (mn).

Equations (14) and (15) can be given as constraints for Eq. (24):

$$F_1(\mathbf{i}^w) = I_0 - \sum_{n=1}^{N_z} \sum_{m=1}^{N_\theta} \Delta S^w_{mn} i^w_{mn} = 0, \tag{29}$$

$$F_2(\mathbf{i}^w, \boldsymbol{\Phi}^w, \boldsymbol{\Phi}^c)_{mn} = i^w_{mn} - i^*(e^{(\phi^c_n - \phi^w_{mn} - \phi^*)/\beta_a} - e^{-(\phi^c_n - \phi^w_{mn} - \phi^*)/\beta_c}) = 0,$$
$$\text{for} \quad m=1, ..., N_\theta \text{ and } n=1, ..., N_z. \tag{30}$$

3.3. *Iterative Schemes*

The system of linear equations of (24) is solved with the boundary conditions of (29) and (30). Due to the nonlinearity of boundary conditions, the following iterative algorithm is devised:

(i) Assume i^w_{mn} (a uniform distribution) and ϕ^c_0 ($=0$).

(ii) Solve Eq. (24) and determine the potential distribution in the formation near the well casing, ϕ^w_{mn}.

(iii) Calculate the current and potential distribution on the well casing surface, $\Im_j$ and ϕ^c_j, from Eqs. (27) and (28).

(iv) Examine the constraint conditions of F_1 and $F_{2,mn}$ as shown in Eqs. (29) and (30).

(v) Update i^w_{mn} and ϕ^c_0 and repeat from (ii) to (iv).

To facilitate numerical convergence, a Newton–Raphson method was derived from Eqs. (29) and (30):

$$-F^{[i]}_1 = \sum_{l_1, l_2} \Delta S^w_{l_1 l_2} \Delta i^{w[i+1]}_{l_1 l_2}, \tag{31}$$

$$-F^{[i]}_{2,mn} = \Delta i^{w[i+1]}_{mn} + \frac{\partial F_2}{\partial \phi^c_n}\left[\sum_{l_1, l_2} \frac{\partial \phi^c_n}{\partial i^w_{l_1 l_2}} \Delta i^{w[i+1]}_{l_1 l_2} + \Delta \phi^{c[i+1]}_0\right] + \frac{\partial F_2}{\partial \phi^w_{mn}} \sum_{l_1, l_2} \frac{\partial \phi^w_{mn}}{\partial i^w_{l_1 l_2}} \Delta i^{w[i+1]}_{l_1 l_2}. \tag{32}$$

Equations (31) and(32) are a system of $(N_z N_\theta + 1)$ linear equations for the $[i+1]$th updates of i^w_{mn} and ϕ^c_0.

The Newton-Raphson iterations continue until the normalized residual,

$$E^{[i]} = \frac{1}{i_{\text{avg}}} \sqrt{\textstyle\sum_{m,n} (F^{[i]}_{2,mn})^2 / N_\theta N_z}, \tag{33}$$

becomes less than 10^{-4}. Owing to the linearity of Eq. (29), $F^{[i]}_1$ remains zero during the iterations.

3.4. *Linear Solver*

In the process of iterations, Eq. (24) is solved repeatedly with an updated right-hand side vector. Owing to the shared boundaries between layers, the matrix becomes a banded block matrix. Therefore, a Schur-complement-like method was devised to solve the matrix efficiently. The numerical algorithm is described in the Appendix.

4. NUMERICAL RESULTS

We first discuss the numerical efficiency of the method and then examine the effects of physical parameters on the solution. The physical parameters for the base model are listed in Table I, and the geometries of well casing models are depicted in Fig. 2. Vertical casing models (Models A, B, and C with single-, two-, and three-layered conductivities, respectively) were mainly used to investigate the effects of

TABLE I

Casing Geometry and Physical Properties

Casing length
Model A, B, C: $L = 1240$ [m]
Model D: $L = 944.43$ [m]
Casing radius, $r_w = 0.08$ [m]
Metal resistivity, $R_s = 10^{-5}$ [Ω/m]
Current source, $I_0 = 5$ [A]
Location of current source, $\mathbf{x}_0 = (200, 0, 0.1)$ [m]
Electrochemical kinetics parameter, $i^* = 0.004$ [A/m^2]
Electrochemical kinetics parameter, $\phi^* = 0.7$ [V]
Electrochemical kinetics parameter, $\beta_a = 0.04$ [V]
Electrochemical kinetics parameter, $\beta_c = 0.04$ [V]
Soil conductivities [$1/\Omega m$]
Model A: $\sigma^{(1)} = 0.1$
Models B and D: $\sigma^{(1)} = 0.0333$, $\sigma^{(2)} = 0.1$
Model C: $\sigma^{(1)} = 0.0333$, $\sigma^{(2)} = 0.1$, $\sigma^{(3)} = 0.01$

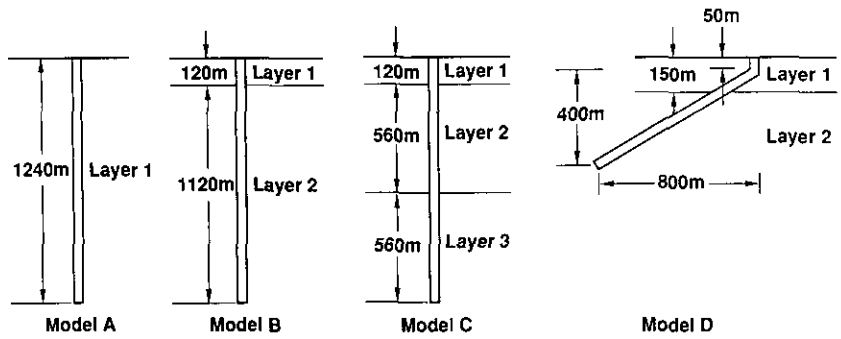

FIG. 2. Model geometries.

conductivities of soil, well casing geometry, well casing resistivity, and the location of a current source on the current distribution at the well casing. Model D was included to demonstrate the importance of the current source location for an arbitrarily deviated casing.

4.1. *Numerical Efficiency and Convergence*

The present numerical method consists of three major parts: (1) the evaluation of potentials (calculation of matrix elements), (2) the LU decomposition of the matrix, and (3) Newton–Raphson iterations to satisfy the nonlinear boundary conditions at the well casing. When the casing remains in the x-z plane, the plane symmetry reduces the matrix size by 50%. Moreover, if uniform grids are used in a vertical casing, many matrix element calculations can also be eliminated due to the grid symmetry. As a result, we utilized proper symmetry conditions to maximize numerical efficiency.

The side surface of the casing was discretized by 4×20 elements, the bottom of the casing by 4×2 elements, and the layer boundary by 8×8 elements. The CPU time required on the VAXstation 3200 was 26.0 s for Model A, 93.7 s for Model B, 156.6 s for Model C, and 99.4 s for Model D. The plane symmetry was used for Model D, whereas both the grid and plane symmetries were used for the other models.

In performing the Newton–Raphson iterations to satisfy the nonlinear boundary conditions, only the right-hand side

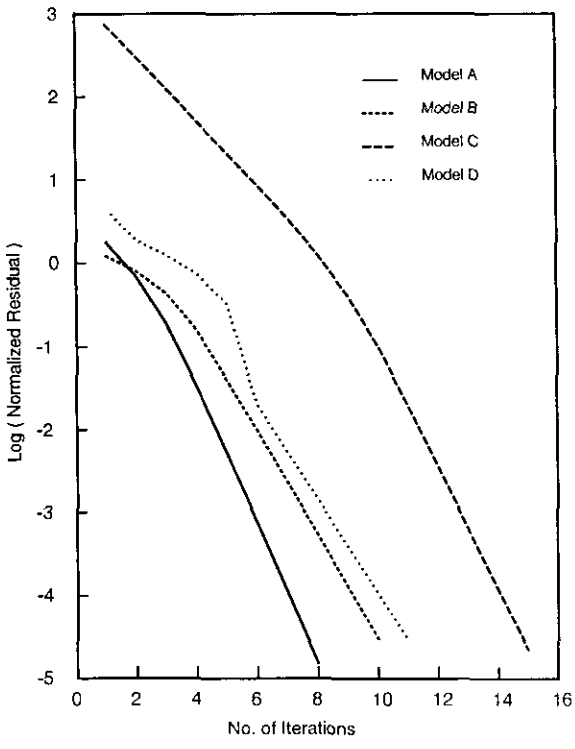

FIG. 3. Convergence of Newton–Raphson iterations.

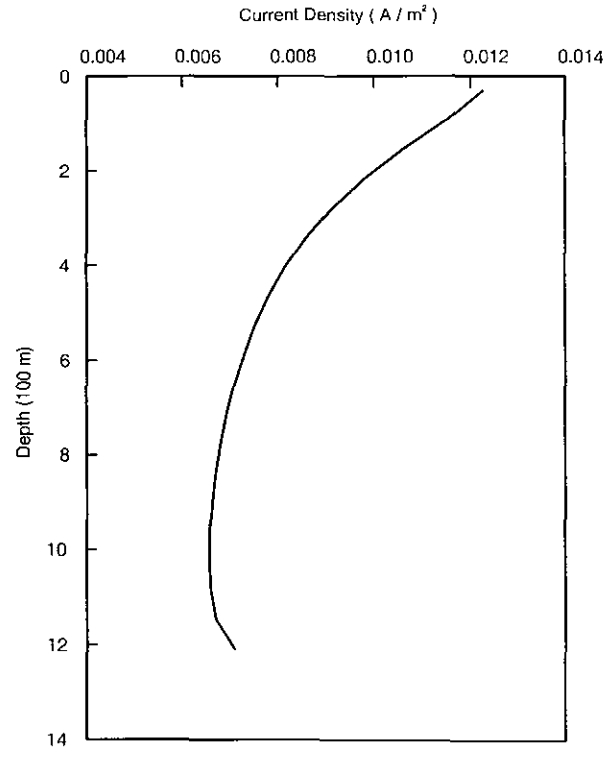

FIG. 4. Current density distribution: Model A, $x_0 = 200$ m.

vector of Eq. (24) has to be modified. Therefore, the iterations can be achieved very effectively once the LU decomposition of the matrix in Eq. (24) is stored. Figure 3 shows the convergence rate of Newton–Raphson iterations for Models A, B, C, and D. The initial estimate of i^w_{mn} was a uniform distribution. In the single-layered Model A, the normalized residual decreased by five orders of magnitude within eight iterations. In Model C with very different layer conductivities, the simple initial estimate of i^w_{mn} generated a large error as shown in Fig. 3. Nevertheless, as the present Newton-Raphson method revealed superlinear convergence, the solution converged within 15 iterations.

4.2. *Single-Layered Model (Model A)*

The current source was located at $\mathbf{x}_0 = (200, 0, 0.1)[m]$ in this single-layered model. The calculated current distribution along the well casing surface is shown in Fig. 4. The current distribution was axisymmetric on the well casing surface (minimal dependency on the azimuthal direction) and reached a maximum at the top of the casing. The current density changed between 0.00657 and 0.01226 $[A/m^2]$ along the axial direction of the casing. It became gradually smaller along the axial direction, but slightly increased again near the end of the casing. A similar end effect has been shown by Dabkowski's model [3], and was also observed in flow in porous media [9].

The same model A with the current source at $\mathbf{x}_0 = (20, 0, 0.1)[m]$ was considered. The simulation results were depicted in Fig. 5. The current was mostly picked up at the top portion of the casing and its distribution became less uniform (0.0049–0.0691 $[A/m^2]$). The current distribution at the top of the casing also showed a weak dependency on the azimuthal direction.

Most previous models neglected the potential changes on the metal surface because the metal conductivity is much larger than that of soil. However, the electrochemical reactions at the casing introduce stiff boundary conditions so that even a minor potential difference in the metal casing can significantly alter the current distribution. In Fig. 6, the current distributions for the cases of R_s (metal resistivity/unit length) $= 10^{-4}$, 10^{-5}, and 10^{-6} $[\Omega/m]$ are plotted. A high metal resistivity generates large potential and current changes on the casing. Figure 6 shows that the potential change in the casing due to the metal resistivity cannot be neglected.

4.3. *Two-and Three-Layered Models (Models B and C)*

A soil formation often consists of multiple layers with different conductivities. Because the numerical algorithm was specifically derived to solve the electrical field for this situation, it is instructive to examine how the current distribution is altered due to a conductivity jump between layers.

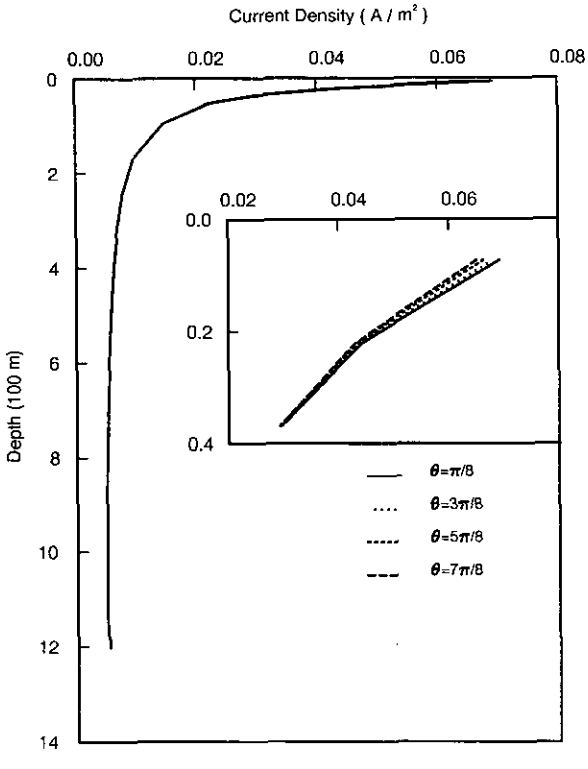

FIG. 5. Current density distribution: Model A, $x_0 = 20$ m.

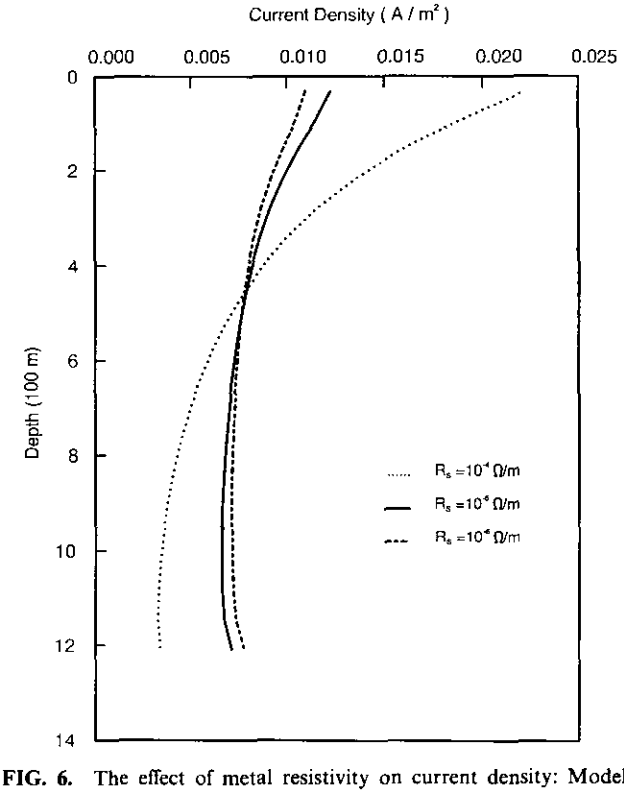

FIG. 6. The effect of metal resistivity on current density: Model A (one layer), $x_0 = 200$ m.

In Model B, the formation has two layers: the top layer of 120 [m] thickness has conductivity $\sigma^{(1)} = 0.0333[1/\Omega m]$, and the second layer has the same conductivity as Model A, $\sigma^{(2)} = 0.1[1/\Omega m]$. Figure 7 shows the current distribution along the axial direction of the casing. The current distribution in the first layer is much smaller than that in the second layer, and the current density jumps from 0.00586 to 0.01278 [A/m^2] at the layer boundary. The current distribution in the second layer appears to be similar to that in the single-layer model (i.e., a high current at the top and a moderate increase at the end).

In the three-layered model (Model C), the layer boundaries are located at 120 [m] and 580 [m] from the top plane surface. The soil conductivities are $0.0333[1/\Omega m]$ in layer 1, $0.1[1/\Omega m]$ in layer 2, and $0.01[1/\Omega m]$ in layer 3. In this case, most of the current is expected to be picked up in layer 2 because of its high conductivity. The simulation results are shown in Fig. 8. Compared with Model B, the current density in layer 1 increased due to lower conducitivity in layer 3. The large contrast in soil conductivities between layers 2 and 3 apparently created the current density jump of 0.0116 [A/m^2] at the layer boundary.

4.4. *A Deviated Casing in a Two-Layered Formation (Model D)*

The previous examples modeled a vertical casing in a multilayered formation. To illustrate an efficient use of the

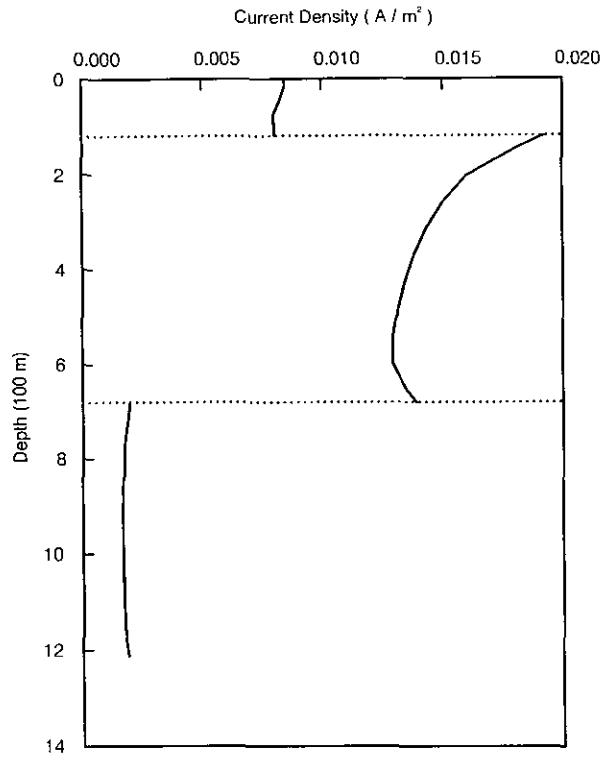

FIG. 8. Current density distribution: Model C (three layers), $\sigma^{(1)} = 0.033$, $\sigma^{(2)} = 0.1$, $\sigma^{(3)} = 0.01$ ($1/\Omega$ m).

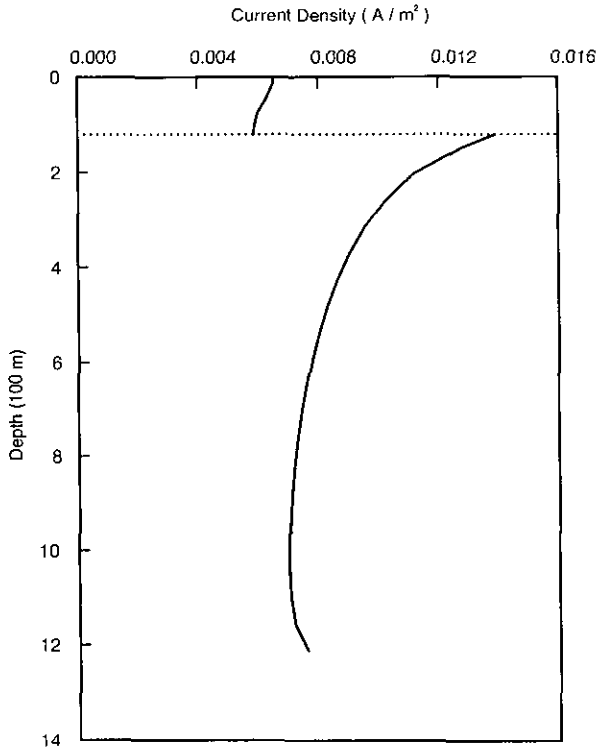

FIG. 7. Current density distribution: Model B (two layers), $\sigma^{(1)} = 0.033$, $\sigma^{(2)} = 0.1$ ($1/\Omega$ m).

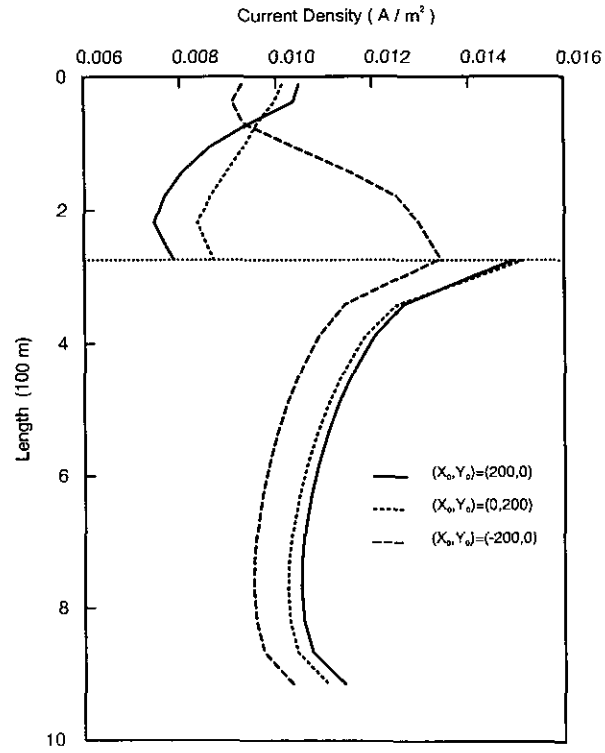

FIG. 9. Current density distribution: Model D (a deviated casing in two layers), $\sigma^{(1)} = 0.033$, $\sigma^{(2)} = 0.1$ ($1/\Omega$ m).

boundary element method for a casing of arbitrary geometry, we designed a well casing that is vertical for the first 120 $[m]$ and then deviates in the x-y plane. The schematic diagram is shown in Fig. 2. The layer conductivities are $\sigma^{(1)} = 0.0333$ and $\sigma^{(2)} = 0.1\,[1/\Omega m]$.

Because this problem is not axisymmetric with respect to the current source location, it is of particular interest to examine its effect on the overall current distribution. Figure 9 shows the current distribution of the three cases: $\mathbf{x}_0 = (200, 0, 0.1)$, $(0, 200, 0.1)$, and $(-200, 0, 0.1)[m]$. The source at $(-200, 0, 0.1)[m]$ distributes current more evenly than the other two cases and exhibits a minor jump at the layer boundary. This numerical example of Model D clearly indicates that the current source location can significantly affect the current distribution in a deviated well casing.

5. CONCLUSIONS

A boundary element method was developed to study cathodic protection of a well casing in a formation with layered conductivities. Electrochemical reactions at the well casing were modeled with a nonlinear Tafel equation [17]. The present formula employs a fundamental solution that eliminates the discretization of the top ground surface. In addition, the model included the potential change in the axial direction of the casing surface due to the metal resistivity. A Newton–Raphson method was employed to satisfy the nonlinear boundary conditions at the well casing. Due to the superlinear convergence of the current algorithm, most practical problems converged within 15 iterations.

Vertical and deviated casing models were constructed to examine the effects of conductivities of soil, well casing geometry, well casing resistivity, and the location of a current source on the current distribution at the well casing. Due to a high aspect ratio of the casing surface ($L/r_w = \sim 1000$), simulation results confirmed a weak dependency on the azimuthal direction of the current distribution on the well casing. The maximum current occurred at the top of the well casing and the current density gradually became smaller along the axial direction, as is found in actual measurements. Nevertheless, near the end of the casing the current slightly increased (a similar end effect was observed in flow in porous media [9]). As the current source was closely located to the casing, the current distribution became less uniform and more current was picked up at the top portion of the casing.

Although the metal conductivity is much larger than that of soil, even a minor potential difference on the casing surface can significantly alter the current distribution owing to the stiff, nonlinear boundary conditions. Furthermore, as the metal resistivity increases, the current distribution becomes less uniform. In the formation with multi-layered resistivities, the current density suffered a jump at the layer boundary. Most of the current was picked up at the casing surface in the layer with a high conductivity. In a deviated casing the location of the source was an important factor in determining the current distribution.

APPENDIX: A SCHUR-COMPLEMENT-LIKE METHOD FOR BANDED BLOCK MATRICES

A multilayered model generates a banded block matrix due to the shared boundaries between layers. In this Appendix, we derive a Schur-complement-like method to solve this matrix efficiently. The matrix from a three-layered model is

$$\begin{pmatrix} A_{11} & A_{12} & A_{1b} & 0 & 0 & 0 & 0 \\ 0 & A_{2a} & A_{21} & A_{22} & A_{23} & A_{2b} & 0 \\ 0 & 0 & 0 & 0 & A_{3a} & A_{32} & A_{33} \end{pmatrix} \times \begin{pmatrix} X_{11} \\ X_{12} \\ X_{21} \\ X_{22} \\ X_{23} \\ X_{32} \\ X_{33} \end{pmatrix} = \begin{pmatrix} B_1 \\ B_2 \\ B_3 \end{pmatrix}. \tag{a1}$$

When the number of grid points on the well casing in layer i is NP_i and the shared boundary between layers i and $(i+1)$ is discretized by NO_i grids, the total number of grids in layer i becomes $N_i = NP_i + NO_i + NO_{i-1}$. Then the dimensions of A_{ii}, $A_{i,i-1}$, $A_{i,i+1}$, A_{ia}, and A_{ib} become $(N_i \times NP_i)$, $(N_i \times NO_{i-1})$, $(N_i \times NO_i)$, $(N_i \times NO_{i-1})$, and $(N_i \times NO_i)$, respectively. For simplicity of notation, we define square matrices as

$$A_1 \equiv (A_{11}, A_{12}), \quad A_2 \equiv (A_{21}, A_{22}, A_{23}), \quad A_3 \equiv (A_{32}, A_{33}), \tag{a2}$$

and group the variables as

$$X_1 \equiv \begin{pmatrix} X_{11} \\ X_{12} \end{pmatrix}, \quad X_2 \equiv \begin{pmatrix} X_{21} \\ X_{22} \\ X_{23} \end{pmatrix}, \quad X_3 \equiv \begin{pmatrix} X_{32} \\ X_{33} \end{pmatrix}. \tag{a3}$$

We further define two matrices that are a combination of an identity matrix and a null matrix:

$$J_i \equiv [O_{NO_i \times (N_i - NO_i)}, I_{NO_i}], \tag{a4}$$

$$K_i \equiv [I_{NO_{i-1}}, O_{NO_{i-1} \times (N_i - NO_{i-1})}]. \tag{a5}$$

Here, I_m is the $m \times n$ identity matrix, and $O_{m \times n}$ is the $m \times n$ null matrix.

From Eqs. (a1)–(a3), the system of linear equations can be more concisely expressed as

$$A_1 X_1 + A_{1b} X_{21} = B_1, \tag{a6}$$

$$A_{2a} X_{12} + A_2 X_2 + A_{2b} X_{32} = B_2, \tag{a7}$$

$$A_{32} X_{23} + A_3 X_3 = B_3. \tag{a8}$$

Equation (a6) can be rearranged to solve for X_1 as

$$X_1 = -A_1^{-1} A_{1b} X_{21} + A_1^{-1} B_1. \tag{a9}$$

The X_{12} that is a subset of X_1 can be conveniently expressed with J_1 and Eq. (a9),

$$X_{12} = J_1 X_1 = -J_1 A_1^{-1} A_{1b} X_{21} + J_1 A_1^{-1} B_1. \tag{a10}$$

Substituting (a10) into (a7), we obtain

$$\tilde{A}_2 X_2 + A_{2b} X_{32} = \tilde{B}_2. \tag{a11}$$

Here,

$$\tilde{A}_2 = -K_2 A_{2a} J_1 A_1^{-1} A_{1b} + A_2, \tag{a12}$$

$$\tilde{B}_2 = B_2 - A_{2a} J_1 A_1^{-1} B_1. \tag{a13}$$

Equation (a11) can be rearraned to solve for X_2 as

$$X_2 = -\tilde{A}_2^{-1} A_{2b} X_{32} + \tilde{A}_2^{-1} \tilde{B}_2 \tag{a14}$$

and X_{23} becomes

$$X_{23} = J_2 X_2 = -J_2 \tilde{A}_2^{-1} \tilde{A}_{2b} X_{32} + J_2 \tilde{A}_3^{-1} \tilde{B}_2. \tag{a15}$$

Finally, substituting (a15) into (a8), we obtain

$$X_3 = \tilde{A}_3^{-1} \tilde{B}_3, \tag{a16}$$

where

$$\tilde{A}_3 = -K_3 A_{3a} J_2 A_2^{-1} A_{2b} + A_3, \tag{a17}$$

$$\tilde{B}_3 = B_3 - A_{3a} J_2 A_2^{-1} B_2. \tag{a18}$$

The numerical algorithm can be summarized as follows. First, the LU decomposition of A_1 is evaluated and then $A_1^{-1} A_{1b}$, and $A_1^{-1} B_1$ are calculated. Second, $\tilde{A}_2$ and $\tilde{B}_2$ are computed from Eqs. (a12) and (a13). After decomposing $\tilde{A}_2$ into LU triangular matrices, $\tilde{A}_3$ and $\tilde{B}_3$ are readily computed from Eqs. (a17) and (a18). Then X_3, X_2, and X_1 are sequentially evaluated from Eqs. (a16), (a14), and (a9).

Even though this Appendix discussed a method for a three-layered model, the same algorithm can be straightforwardly extended to a model with any number of layers.

REFERENCES

1. R. Pope, *Corrosion* **2**, 307 (1946).
2. F. W. Schremp and L. E. Newton, *Corrosion 79* (1979); Paper No. 63, National Association of Corrosion Engineers, Houston, Texas.
3. J. Dabkowski, Final Report PR-151-106, American Gas Assoc., 1983.
4. C. A. Brebbia, *Progress in Boundary Element Methods*, Vol. 1, (Wiley, New York, 1981), Vol. 2, (Prentech, New York, 1983).
5. J. J. Connor and C. A. Brebbia, *Betech 86*, (Comput. Mech., Billerica, MA, 1986).
6. S. H. Lee and L. G. Leal, *J. Colloid Interface Sci.* **87**, 81 (1982).
7. A. S. Geller, S. H. Lee, and L. G. Leal, *J. Fluid Mech.* **169**, 27 (1986).
8. J. A. Liggett and P. L.-F. Liu, *The Boundary Integral Equation Method for Porous Media Flow*, (Allen & Unwin, London, 1983).
9. S. H. Lee, *SPE Product. Eng.* **4**, 173 (1989).
10. J. C. F. Telles, W. J. Mansur, W. J. Wrobel, and M. G. Marinho, *Corrosion 89* (1989), Paper No. 276, National Association of Corrosion Engineers, New Orleans, LA.
11. P. Chauchot, B. Bigourdan, and L. Lemoine, *Corrosion 89* (1989), Paper No. 401, National Association of Corrosion Engineers, New Orleans, LA.
12. N. G. Zamani and J. F. Porter, in *Proceedings of the Int. Conf. on Boundary Element Technology BETECH 87*, edited by C. A. Brebbia, p. 123.
13. R. Strommen, W. Keim, J. Finnegan, and P. Mehdizadeh, *Mat. Perform.* **26**, 23 (1987).
14. I. Stakgold, *Green's Functions and Boundary Value Problems*, (Wiley, New York, 1979).
15. E. P. Ascoli, D. S. Dandy, and L. G. Leal, *Int. J. Num. Methods Fluids* **9**, 651 (1989).
16. N. M. Günter, *Potential Theory and its Applications to Basic Problems of Mathematical Physics*, (Ungar, New York, 1967).
17. H. H. Uhlig, *Corrosion and Corrosion Control*, (Wiley, New York, 1971).
18. L. V. Kantorovich and V. I. Krylov, *Approximate Methods of Higher Analysis*, (Interscience, New York, 1958).